Microstructural Evolution of the Nickel Platinum–Aluminide Bond Coat on Electron-Beam Physical-Vapor Deposition Thermal-Barrier Coatings during High-Temperature Service

L.C. ZHANG and A.H. HEUER

The microstructural evolution of a (Ni,Pt)-aluminide bond coat underneath the ZrO_2-based thermal-barrier coating (TBC) topcoat system on a René N5 Ni-based superalloy turbine blade during prolonged high-temperature service has been characterized using transmission electron microscopy (TEM). The as-deposited bond coat has a spatially varying microstructure, which consists of an outer layer of single-phase β-(Ni,Pt)Al, a middle layer of a β-(Ni,Pt)Al matrix containing a high number density of μ-phase precipitates, and an inner layer containing a γ/γ' matrix and numerous μ- and σ-phase precipitates. During service, microstructural changes in the hotter sections of the blade are more extensive than those in the cooler parts, as expected. As a result of interdiffusion, the inner layer grows into the γ/γ' substrate, with the formation of some $M_{23}C_6$ precipitates, and the β matrix in the middle layer is transformed into a two-phase mixture of β and γ'. Corresponding changes occur in the morphologies and volume fractions of the various precipitate phases present in the bond coat. The single-phase β material in the outer layer retains its basic structure, except that the compositional changes due to diffusion between the bond coat and turbine blade cause a martensitic transformation to occur in the hottest sections during the final cooling of the blade. The distribution of various elements in the different layers has also been analyzed, as has growth of the thermally grown oxide (TGO) at the bond coat/TBC interface.

I. INTRODUCTION

IT is well known that modification of Ni-aluminide bond coats by Pt additions significantly improves their resistance to high-temperature oxidation and hot corrosion.[1–4] Such property enhancements have led to widespread application of Pt-aluminide bond coats on superalloy components of advanced gas turbine engines. Some studies[5–8] have indicated several coupled effects of the Pt addition in these Ni-aluminide bond coats. First, Pt increases the coating stability by preventing inward diffusion of Al and outward diffusion of Ni and refractory elements like Mo, V, Ta, and W.[5] Second, Pt increases the diffusivity of Al in the outer region of the bond coat, resulting in the formation of a purer thermally grown oxide (TGO).[6] In addition, Pt improves oxide adherence.[7,8] Last, Pt prevents the β-NiAl alloy from transforming into a γ'-Ni_3Al–based alloy, thereby improving the oxidation resistance of the bond coat.[6]

The aluminide bond coats deposited on single-crystal superalloy turbine blades involve several matrix and precipitate phases, primarily β-NiAl and γ'-Ni_3Al matrix phases and μ, σ, and σ' precipitates (the superalloy substrate itself is, of course, a γ/γ' Ni-based alloy). Precipitation of the μ and σ phases usually depletes the substrate of the refractory strengthening elements Ta, W, Mo, Cr, and Co and can, therefore, be detrimental to mechanical properties of the superalloy. However, these precipitates do have a beneficial effect on coating stability by restricting inward diffusion of Al and outward diffusion of Ni.[9] It is worth noting that the μ phase preferentially dissolves W and Ta and the σ phase preferentially dissolves Cr and Co. Furthermore, α-Cr precipitates are commonly encountered in the simple aluminide bond coat,[10] whereas α-W precipitates have been found in a Pt-aluminide bond coat,[11] where they formed by outward diffusion of W from the superalloy substrate. Carbide precipitates are present in some bond coats when sufficient carbon is present.[12]

In order to investigate the mechanisms of degradation of these bond coats, laboratory studies have been carried out involving isothermal exposure,[10,13–15] thermal fatigue,[15] and thermomechanical fatigue[16] under various conditions. All these studies have shown that two processes dominate the microstructural evolution: interdiffusion between the bond coat and substrate and oxidation of the bond coat, leading to the so-called TGO layer beneath the ZrO_2-based thermal-barrier coating (TBC) topcoat. Microstructural characterizations of aluminide bond coats have been published,[10–19] but detailed investigation in terms of phase distribution and phase chemistry is another matter. In this study, we have characterized an actual turbine blade (provided by General Electric (GE) Aircraft Engines) taken out of service after some unknown but modest fraction of life, which clearly experienced a relatively complicated combination of hot deformation and thermal cycling, and compared its microstructure with laboratory coupons, both as-deposited and after a high-temperature exposure. (The Y_2O_3-stabilized ZrO_2 topcoat had been made by electron-beam physical-vapor deposition. Our study complements recent work by Wright, Hemker, and co-workers[20–24] on laboratory coupons of similar composition and structure.

To the best of our knowledge, no similar studies on the microstructure of actual blades taken out of service have been reported to date; our work should help in understanding the factors determining the life of these exquisitely engineered structures.

L.C. ZHANG, formerly Research Associate with the Department of Materials Science and Engineering, Case Western Reserve University, is Postdoctoral Researcher, University of Connecticut, Storrs, CT 06269-3136. A.H. HEUER, University Professor and Kyocua Professor of Ceramics, is with the Department of Materials Science and Engineering, Case Western Reserve University, Cleveland, OH 44106-7204. Contact e-mail: heuer@case.edu

Manuscript submitted December 17, 2003.

II. EXPERIMENTAL PROCEDURE

The laboratory coupon consisted of an electron-beam physical-vapor-deposited 7 w/o Y_2O_3-stabilized ZrO_2 TBC on top of a Pt-modified aluminide bond coat and a René N5 single-crystal substrate; the coupon had been processed identically to production superalloy turbine blades. These turbine blades are manufactured by conventional single-crystal casting technologies. Following casting, and certain proprietary aging heat treatments and proprietary machining operation, the blade was coated with the platinum-aluminide bond coat to provide environmental protection. The PtAl coating was applied in two steps: Pt deposition and aluminiding. A thin layer of Pt was applied to the desired surfaces by electroplating after the surface was cleaned and activated. The thickness of the Pt electroplate was set to achieve the desired postaluminiding composition. The Pt-plated turbine blade was then aluminided using a chemical-vapor deposition process designed to create an "outward" coating. In this process, the Al activity and process temperature are adjusted to promote the outward diffusion of Ni from the substrate to react with Al diffusing in from the coating atmosphere. The coating produced is conventionally described as consisting of two layers: an "additive layer" adjacent to the external surface (termed as such because much of this layer adds to the dimensions of the component) and an interdiffusion zone within the alloy. This low-activity coating process produces a single-phase PtAl coating, where the additive layer of the coating is single-phase β-NiAl (B2 structure) with Pt in solid solution. (This structure is in contrast to so-called higher-activity processes, where the additive layer may contain precipitates of $PtAl_2$ phases due to higher Al levels.)

The shape of the actual blade we studied is similar to that shown in Figure 1. We arbitrarily labeled and sectioned various parts of the blade: sections A, C, E, and G are from the hotter, higher-pressure side of the engine, while sections B, D, F, and H are from the cooler side; sections G and I are close to the leading edge. In this article, we will focus on the cooler section F and the hotter section A, which represent extremes in the thermal exposure, but we will supplement our description with data from other sections, as needed, to fully illustrate the microstructural evolution.

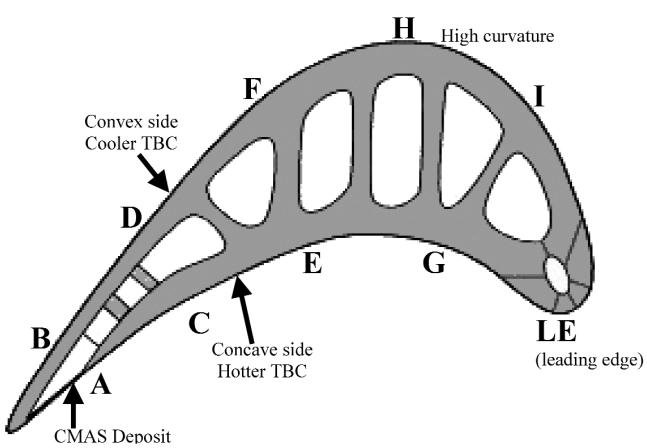

Fig. 1—A schematic diagram of a turbine blade and the various sections that have been studied.

Specimens for scanning electron microscopy (SEM) investigations were prepared by mechanical grinding and polishing. Some specimens were etched using a solution of 97 pct hydrochloric acid (HCl), 2 pct sulfuric acid (H_2SO_4), and 1 pct nitric acid (HNO_3). After the bond coat was etched, the grain boundaries, as well as the β-NiAl and γ'-Ni_3Al phases, could readily be imaged in a PHILIPS* XL-30 environmental SEM (ESEM) with a Noran Vantage energy-dispersive spectroscopy (EDS) system. Volume fractions and sizes of phases visible in the SEM images were analyzed using digital image analysis. Cross-sectional foils for transmission electron microscopy (TEM) were obtained using the technique described by Unal *et al.*,[25] with final thinning using a Gatan precision ion-polishing system. The TEM foils were examined using a PHILIPS CM-20 TEM apparatus operating at 200 kV.

*PHILIPS is a trademark of Philips Electronic Instruments Corp., Mahwah, NJ.

Compositional data were obtained in the transmission electron microscope using a high-purity GE X-ray energy-dispersive spectroscopy (XEDS) detector and the thin-film ZAF-corrected software program in the Noran Voyager EDS system. All compositions are quoted in atomic percent.

III. RESULTS

A. *Microstructure*

Figure 2(a) is a relatively low-magnification cross-sectional SEM image of the as-deposited coupon sample, and Figures 2(b) and (c) are similar images of sections F and A of the used blade; the Al_2O_3 TGO is at the top of each image, and the Renè N5 single-crystal substrate is at the bottom. These images suggest a subdivision of the bond coat into three regions: an inner layer, adjacent to the γ/γ' blade; a middle layer; and an outer layer beneath the Al_2O_3 TGO, itself between the bond coat and the Y_2O_3-stabilized ZrO_2 top coat. During the processing of the bond coat, described earlier, occasion is had to grit blast the exposed surface with Al_2O_3 media, some of which is imbedded in the sample. The residual Al_2O_3 grit particles appear to delineate the transition between the outer and middle layers. We show a further TEM image of these grit particles subsequently.

Various phases within the bond coat are identified by numbers adjacent to the images, the identification being made by TEM (to be discussed subsequently). Measurement of the grain size in various layers performed through SEM imaging on etched-plan and sectional-view samples (images not included here) indicated that the grain size of the outer and middle layers differed significantly. This is clear from Figure 2(d), a backscattered SEM image of a cross section of section A. In this image, the atomic-number contrast renders the β-NiAl phase a lighter shade of gray than the γ'-Ni_3Al phase, while the various precipitate phases to be discussed next are the brightest features in the image. In addition, in the outer layer of hot sections A and C, small γ' intergranular precipitates between the β grains were frequently observed.

A TEM image of the inner layer in the as-deposited material is shown in Figure 3(a). The γ' matrix in the bond coat contains fine precipitates of both σ and σ'; these phases have similar chemistries, as shown in Table I, but are distinctly different crystallographically. The σ phase has tetragonal symmetry,

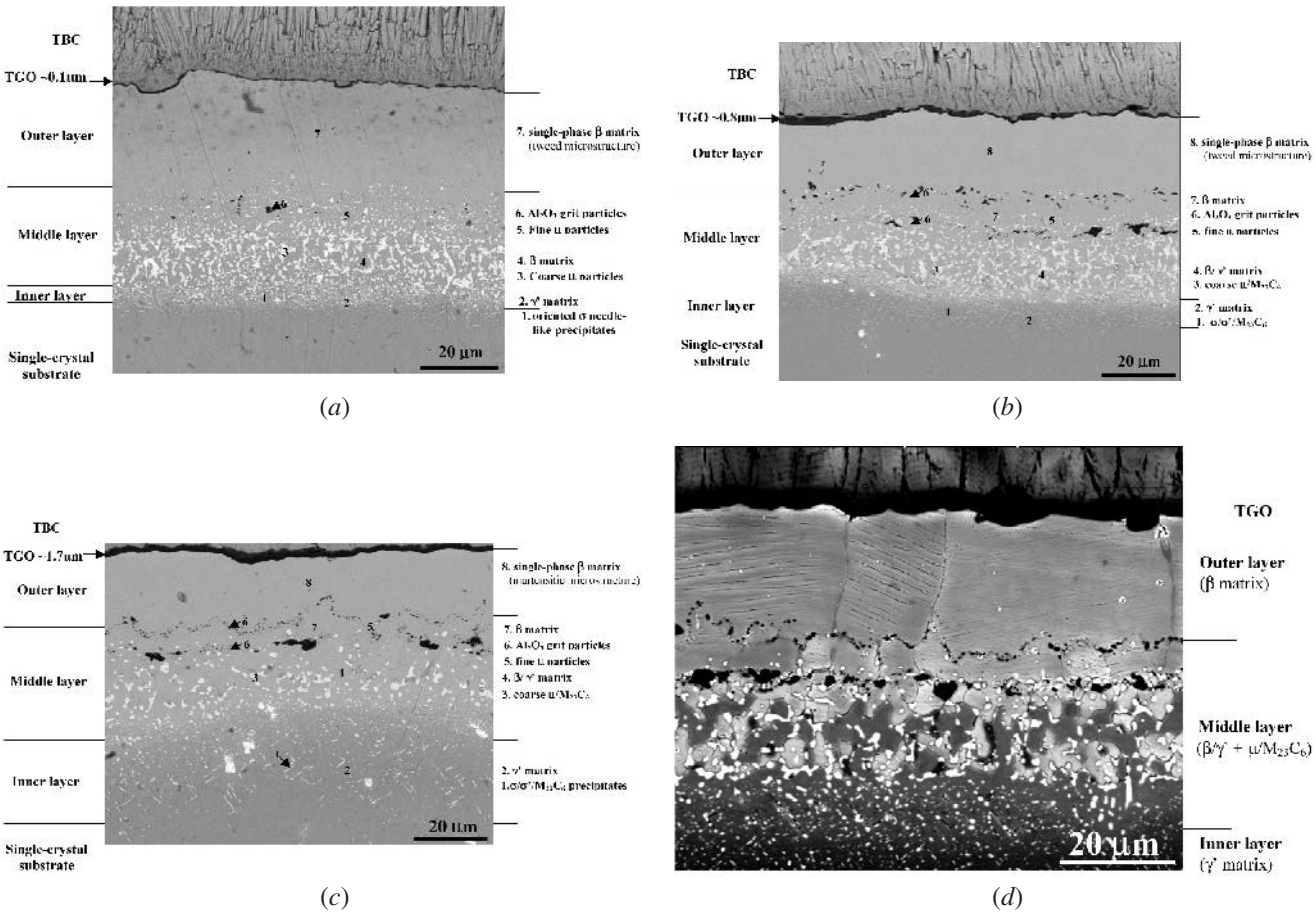

Fig. 2—SEM images showing the main microstructural features of a cross section of the bond coat in (*a*) the as-deposited sample, (*b*) the cooler part F, and (*c*) the hotter part A. (*d*) Backscattered SEM image from Section A.

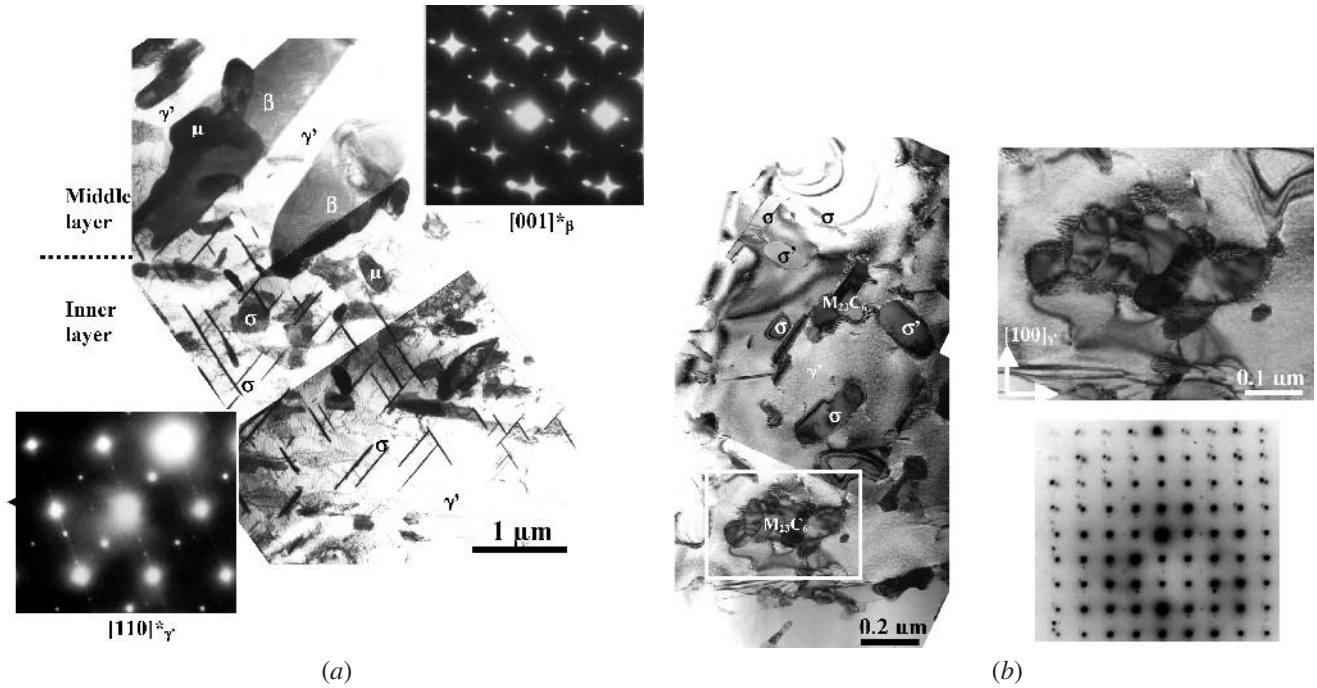

Fig. 3—TEM images. (*a*) the multiphase microstructure in the inner and middle layers in the as-deposited sample. The diffraction patterns from the β and γ' phases are also displayed. (*b*) Numerous precipitates in the extended inner layer of the cooler part F, an enlargement of the framed area showing an $M_{23}C_6$ particle, and its diffraction pattern.

Table I. Chemical Compositions (in Atomic Percent) of Different Phases in the Platinum-Modified Bond Coat

Phases	Elements	Samples		
		As-Deposited Sample	Cool Section F	Hot Section A
Matrix (outer layer)	"β-NiAl"	$Ni_{45}Al_{26}Pt_{14}Co_7Ta_5Cr_2$	$Ni_{44}Al_{25}Pt_{14}Ta_7Co_5Cr_3W$	$Ni_{50}Al_{22}Pt_{13}Ta_5Co_5Cr_4$
Ppts (outer layer)	Al_2O_3	Not present	$Al_{40}O_{57}Ni_2$(W, Ta, Cr, Fe)$_1$	—
Matrix (middle layer)	"β-NiAl"	$Ni_{49}Al_{23}Pt_9Ta_9Cr_5Co_5$	$Ni_{50}Al_{27.5}Pt_{12}Co_5Cr_4WFe$	$Ni_{53}Al_{22}Pt_{10}Co_6Cr_3WFe$
	γ'-Ni_3Al	not present		$Ni_{60}Al_{15}Ta_6Co_5Pt_3Cr_4$
Ppts (middle layer)	μ	$Cr_{21}Ni_{20}W_{15}Co_{14}Ta_{12}Re_9$ Mo_6Pt_3	$Cr_{20}Ni_{17.5}W_{13}Co_{15}$ $Ta_{13}Re_{10}Mo_7Pt_3$	$Cr_{20}Ni_{21}W_{13}Co_{14}Ta_{12}Re_9$ Mo_6Pt_3
	$M_{23}C_6$	not present	—	—
Matrix (inner layer)	γ'-Ni_3Al	$Ni_{60}Al_{16}Ta_9Co_7Pt_4Cr_3W_2$	$Ni_{66}Al_{13}Ta_7Co_6Pt_3W_2Cr_3$	$Ni_{61}Al_{16}Ta_7Co_5Pt_3Cr_3W_2$
Ppts (inner layer)	σ	—	$Cr_{44}Ni_{17}Co_{15.5}W_9Re_8Mo_6$	$Cr_{45}Ni_{17}Co_{16}W_8Re_7Mo_5$
	σ'	—	$Cr_{42}Ni_{16}Co_{14}W_{10}Re_{10}Mo_6Fe$	—
	μ	$Cr_{23}Ni_{18}W_{15}Co_{15}Ta_{12}Re_8$ Mo_6Pt	—	$Cr_{26}Ni_{18}W_{14}Co_{16}Ta_{10}Re_8$ Mo_8Pt
	$M_{23}C_6$	not present	$Cr_{74}Ni_6W_5Re_4Ta_4Co_3Mo_2Pt$	$Cr_{73}Ni_7W_5Re_5Ta_4Co_3Mo_2Pt$
Substrate	γ	$Ni_{50}Cr_{17}Co_{13}Ta_7W_4A_{13}Re_3$ Mo_1Pt	$Ni_{48}Cr_{18}Co_{14}Ta_6W_3Al_3Re_4$ Mo_2Pt	$Ni_{50}Cr_{20}Co_{11}Ta_5W_3Al_7$ Re_2Mo
	γ'	$Ni_{67}Al_{12}Ta_8Co_4W_3Cr_3Pt$	$Ni_{68}Al_1Ta_7Co_5W_4Cr_4Pt$	$Ni_{66}Al_{15}Ta_7Co_5W_3Cr_3Pt$

with $a \sim 0.90$ nm and $c \sim 0.465$ nm, and is a well-known phase in Ni-based alloys.[11,12] To the best of our knowledge, σ' has not been described before; it is orthorhombic with $a \sim 0.102$ nm, $b \sim 0.83$ nm, and $c \sim 0.475$ nm. The Appendix describes the TEM crystallographic characterization of this phase.

As seen in Figure 3(a), the σ phase occurs as needlelike precipitates, whereas σ' appears as blocky precipitates. Blocky μ-phase particles, also well known in Ni-based alloys,[11,12] are present near the inner-layer/middle-layer boundary; we refer to them as particles and not precipitates, as there is no well-defined orientation relationship with the γ' matrix.

It was most convenient to determine the chemistry and crystallography of the σ- and σ'-phase precipitates from the used blade, where the larger size of the precipitates facilitated their characterization. Figure 3(b) shows a portion of the inner layer in section F. All of the σ and σ' precipitates have coarsened, the σ phase losing its characteristic needlelike morphology. The orientation relationships of the σ and σ' precipitates with the γ' matrix are as follows:

$$(2\text{-}20)_{\gamma'}//(1\text{-}10)_{\sigma},\ [001]_{\gamma'}//[110]_{\sigma} \quad [1]$$

$$(1\text{-}11)_{\gamma'}//(001)_{\sigma'},\ [110]_{\gamma'}//[110]_{\sigma'} \quad [2]$$

$$(1\text{-}11)_{\gamma'}//(001)_{\sigma'},\ [110]_{\gamma'}//[140]_{\sigma'} \quad [3]$$

Interestingly, two distinctly different crystallographic orientation relationships (Eqs. [2] and [3]) can be discerned between the σ' precipitates and the γ' matrix. They share the same planar orientation relationship, $(1\text{-}11)_{\gamma'}//(001)_{\sigma'}$, but different directional orientation relations. However, there are no recognizable differences in morphologies between these two types of precipitates.

$M_{23}C_6$ carbide precipitates with a complex subgrain structure are now present; a higher-magnification view of one precipitate is shown in the inset of Figure 3(b). The orientation relation between the $M_{23}C_6$ precipitate and the γ' matrix is given by

$$(100)_{\gamma'}//(100)_{M_{23}C_6} \text{ and } [001]_{\gamma'}//[001]_{M_{23}C_6} \quad [4]$$

The precipitate microstructure in the inner layer in the hottest section A is similar to that in the cooler section F, except that even more precipitate coarsening has occurred in section A than in section F.

Portions of the middle layers in the as-deposited sample and in section F are shown in Figures 4(a) and (b), respectively. The matrix is a β-NiAl phase containing μ particles in the as-deposited sample and a β/γ' matrix containing μ particles and $M_{23}C_6$ precipitates in section F of the blade. The transformation of β to a β/γ' mixture is a consequence of the changing chemistry induced by interdifussion during service.

Portions of the outer layers in sections F and A are shown in Figures 5(a) and (b), respectively. In section F, the matrix contains a "tweed" microstructure, indicative of the well-known structural instability in β-NiAl alloys, in which a tweed morphology often develops on cooling Ni-rich NiAl alloys with the B2 structure. It is generally considered to develop as a precursor to a martensitic transformation and reflects an aperiodic distortion of the lattice on the scale of some tens of atomic spacings. This lattice distortion leads to a characteristic streaking of $\{110\}_{B2}$ reflections in electron diffraction patterns, in addition to the tweed contrast in TEM images.

In the hottest sample we examined, section A, the chemistry has changed sufficiently that the matrix has undergone a martensitic transformation on final cooling to room temperature; diffraction patterns of seven tetragonal martensite variants identified in Figure 5(b) are shown in Figure 5(c).

As noted in Figure 2, grit particles of Al_2O_3 are present within the bond coat;[26] these grit particles more or less define the boundary between the middle and outer layers of the bond coat, as they become embedded in the bond coat. Figure 6 is a TEM micrograph showing these particles in section B.

The second form of α-Al_2O_3 that is present is the TGO, which plays a crucial role in the lifetime of these TBCs. The variable nature of the TGO in the as-deposited material—a columnar α-Al_2O_3 zone and a fine-grained mixed zone of α-Al_2O_3 and ZrO_2—has been shown in earlier work by our group and by others.[27,28] The formation of this mixed zone has been extensively discussed;[25,27–33] the mechanism of its formation is still a matter of debate. The EDS data (not included

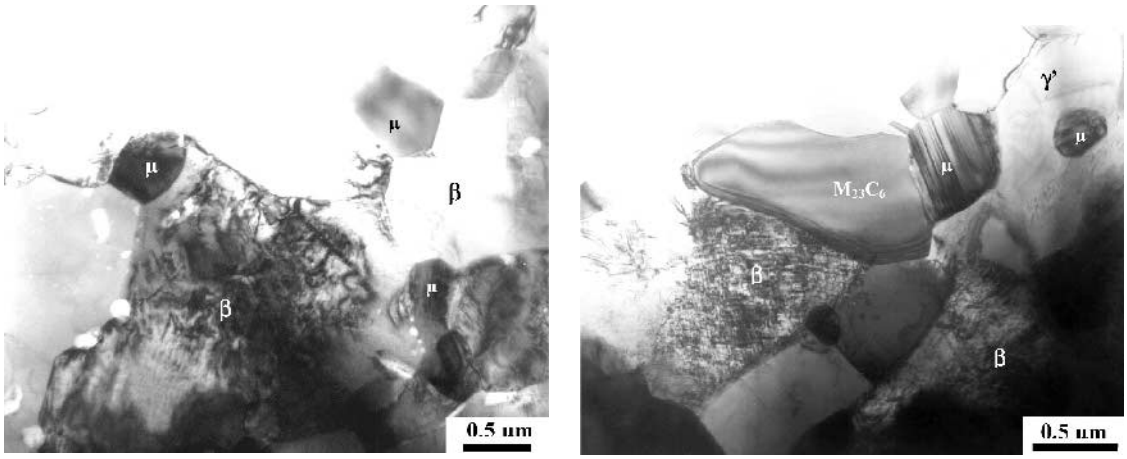

(*a*) (*b*)

Fig. 4—Bright-field TEM micrographs of the middle layer (*a*) in the as-deposited material and (*b*) in section F.

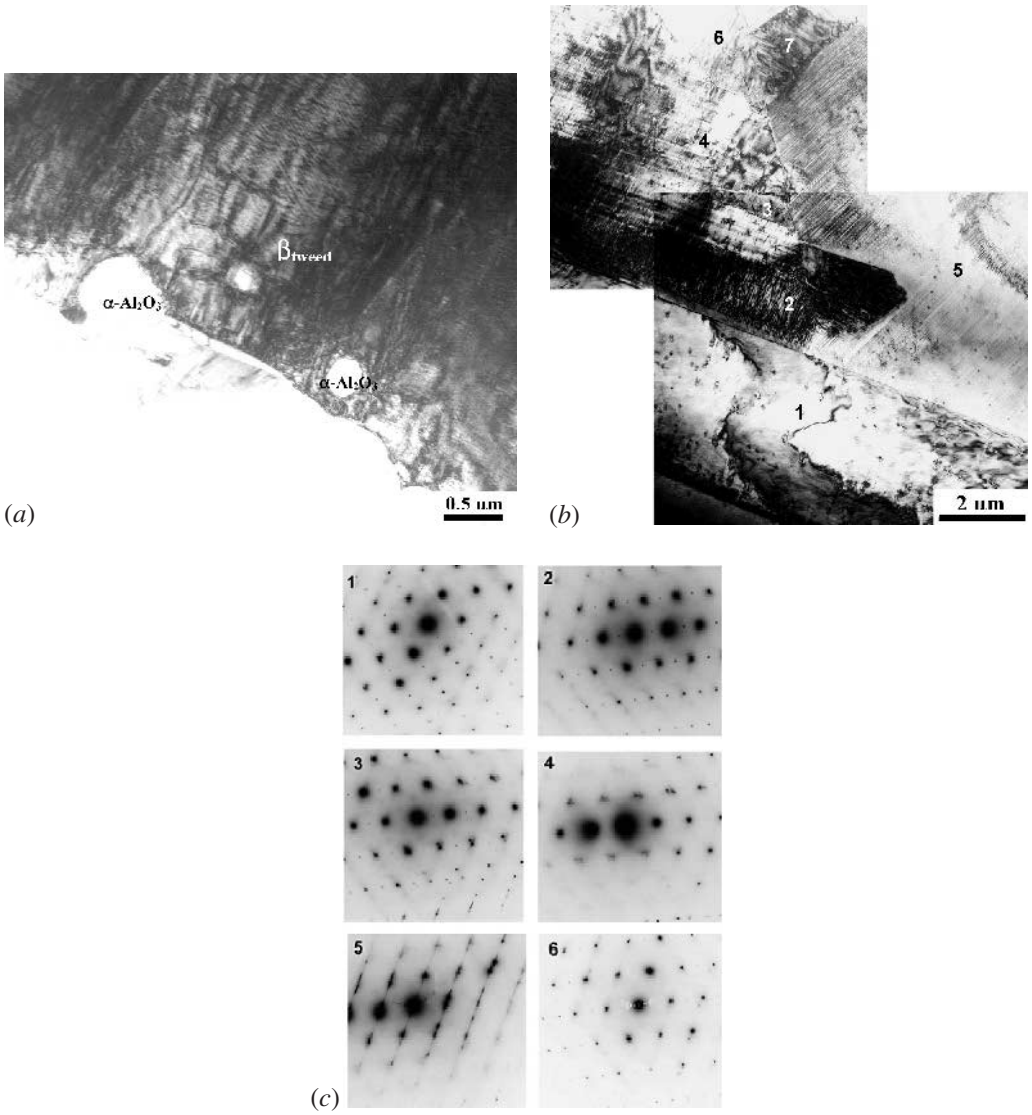

(*a*) (*b*) (*c*)

Fig. 5—Bright-field TEM micrographs of the outer layer in sections (*a*) F and (*b*) A. Diffraction patterns of the seven martensite variants labeled in (b) are shown in (c).

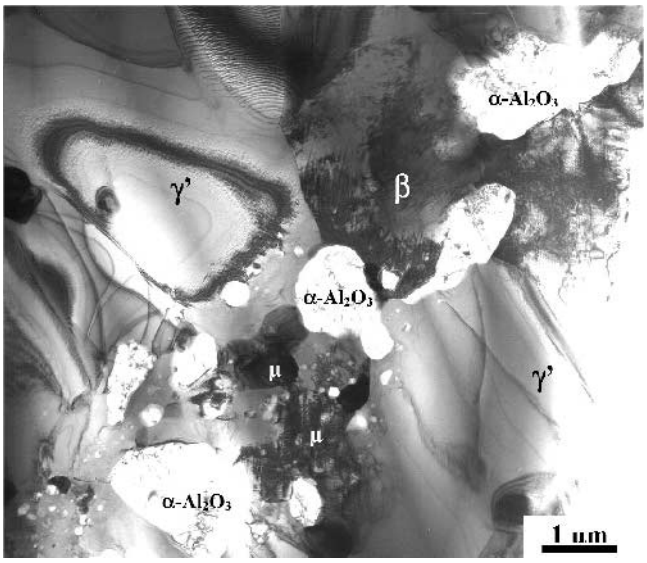

Fig. 6—Bright-field TEM micrograph showing α-Al_2O_3 grit particles incorporated in the bond coat in Section B.

here) confirm that the fine-grained zone contains a mixture of Al_2O_3 and ZrO_2.

Images of the TGO from sections A and B are shown in Figures 7(a) and (b), respectively. Both images clearly show that the newly formed oxide is columnar. In all images from the used blade, the columnar Al_2O_3 layer is "sandwiched" between a fine-grained mixed zone of Al_2O_3 and ZrO_2 and the ZrO_2 topcoat.

We have also determined the average thickness of the TGO at the various positions around the blade, as well as the average dimensions of the columnar Al_2O_3; these data are shown in Table II.

B. *Chemical Evolution*

Figure 8(a) is a schematic drawing of a cross section of the TBC system, summarizing the main changes that occur during high-temperature exposure of the turbine blade. Aside from growth of the TGO by oxidation of the β-NiAl outer layer, Ni outward diffusion occurs from the γ/γ' turbine blade, and Pt inward diffusion occurs toward the substrate. The inner layer, which is a mixture of γ' and β-NiAl with a tweed microstructure and containing σ, σ', and μ phases in the as-received sample, transforms to a γ' matrix in the used blade; the σ, σ', and μ phases coarsen, and $M_{23}C_6$ carbides form.

The middle layer, which is a β-NiAl phase containing μ particles in the as-deposited material, transforms to a β/γ' matrix containing coarse μ particles and $M_{23}C_6$ precipitates. Depending on the position, the β phase can have a tweed substructure or will have undergone a martensitic transformation on cooling. Likewise, the outer β layer has either a tweed or martensitic substructure, depending on the temperatures experienced during service.

Figure 8(b) shows diffraction patterns from β-NiAl in the outer layer from various sections around the blade, along with the *c/a* ratios deduced from this data. This structural evolution can be understood with the assistance of Figure 8(c), which shows the change in the unit cell as the structure transforms from β-NiAl to γ'-Ni_3Al. The B2 structure of NiAl is shown

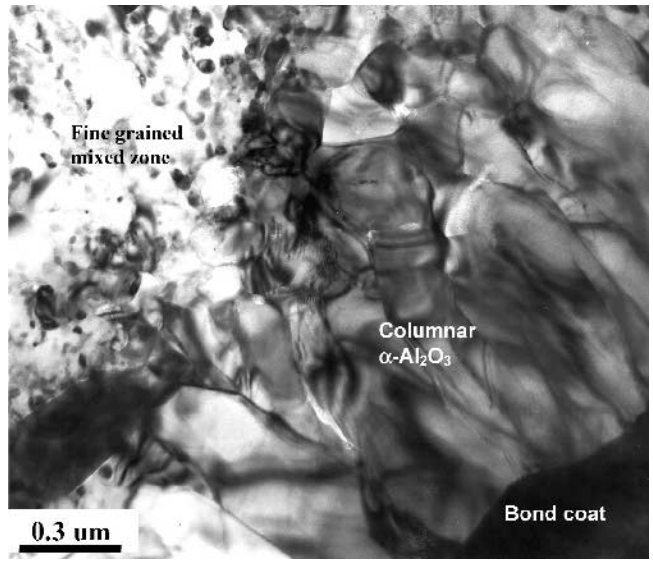

(*a*)

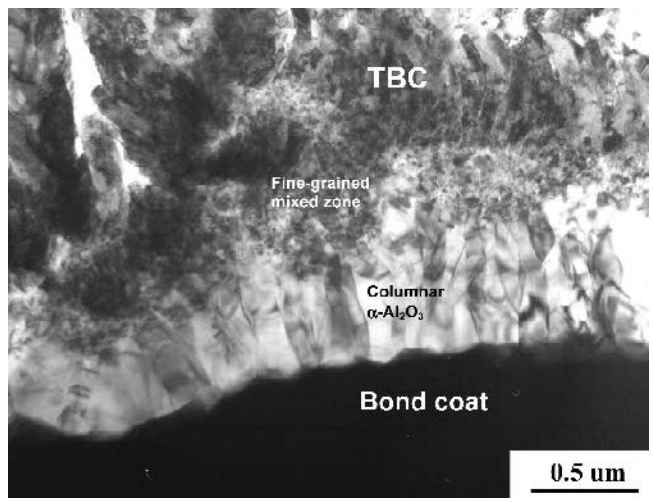

(*b*)

Fig. 7—Bright-field TEM micrographs of the α-Al_2O_3 TGO in Sections (*a*) A and (*b*) B.

Table II. The Average Dimensions of the TGO and the Columnar Al_2O_3 at the Various Positions around the Blade

Section	Average Thickness of Inner Layer (μm)	Average Thickness of TGO (μm)	Average Columnar Dimensions in TGO (Width × Height) (μm)
A	~27	~0.7	~0.1 × ~1.0
B	~18	~1.3	~0.1 × ~0.6
C	~23	~1.4	~0.1 × ~0.6
D	ND*	ND	~0.1 × ~0.5
E	~10	~1.2	~0.1 × ~0.2
F	~6	~0.9	~0.1 × ~0.2
G	~5	~1.0	~0.1 × ~0.1
H	ND	ND	ND
I	~15	~1.4	~0.1 × ~0.5

*ND—not determined

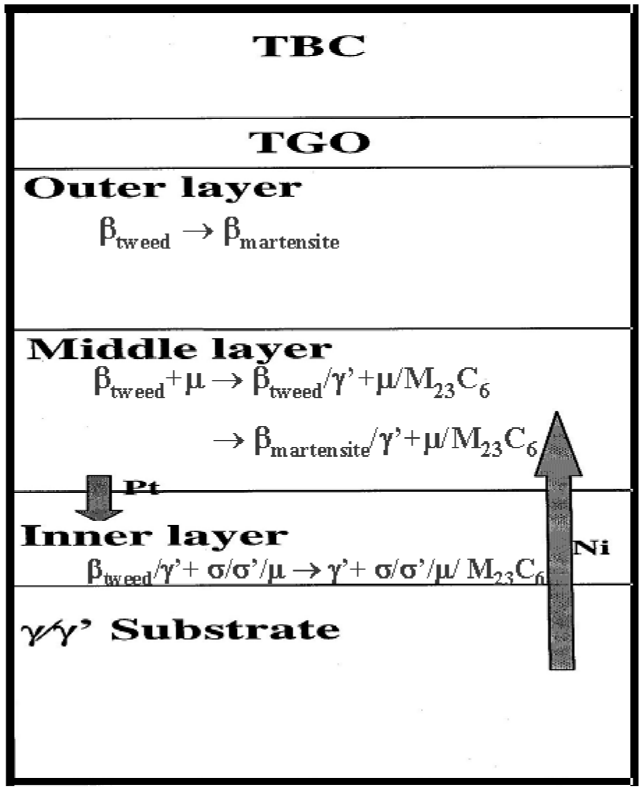

(*a*)

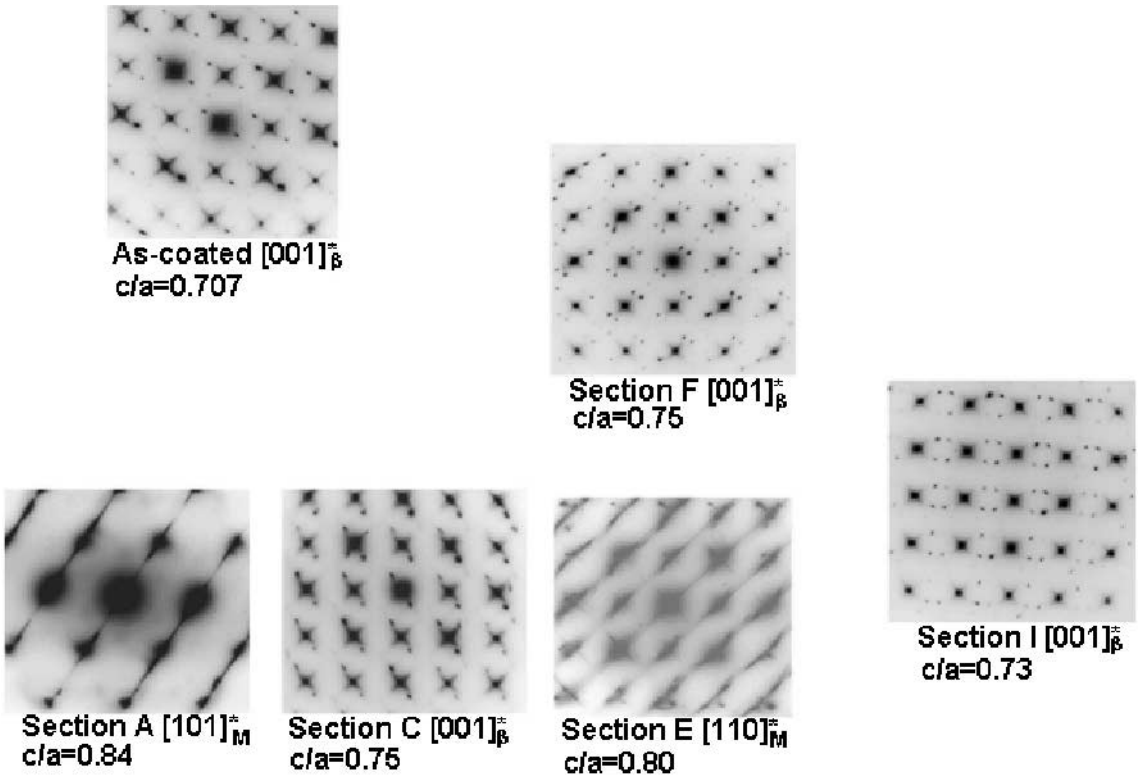

(*b*)

Fig. 8—(*a*) Schematic drawing showing interdiffusion in the bond coat during service; diffraction patterns from β-NiAl in the outer layer from various sections are shown in (*b*), while (*c*) shows schematic drawings of the transition from β-NiAl (B2 structure) to γ'-Ni_3Al (Ll_2 structure). Of course, the martensite and Ni_5Al_3 will have some Ni atoms randomly occupying Al sites, and not the 1:1 stoichiometry shown here. (*d*) Composition profiles through the bond coat for the as-deposited material and for Section A.

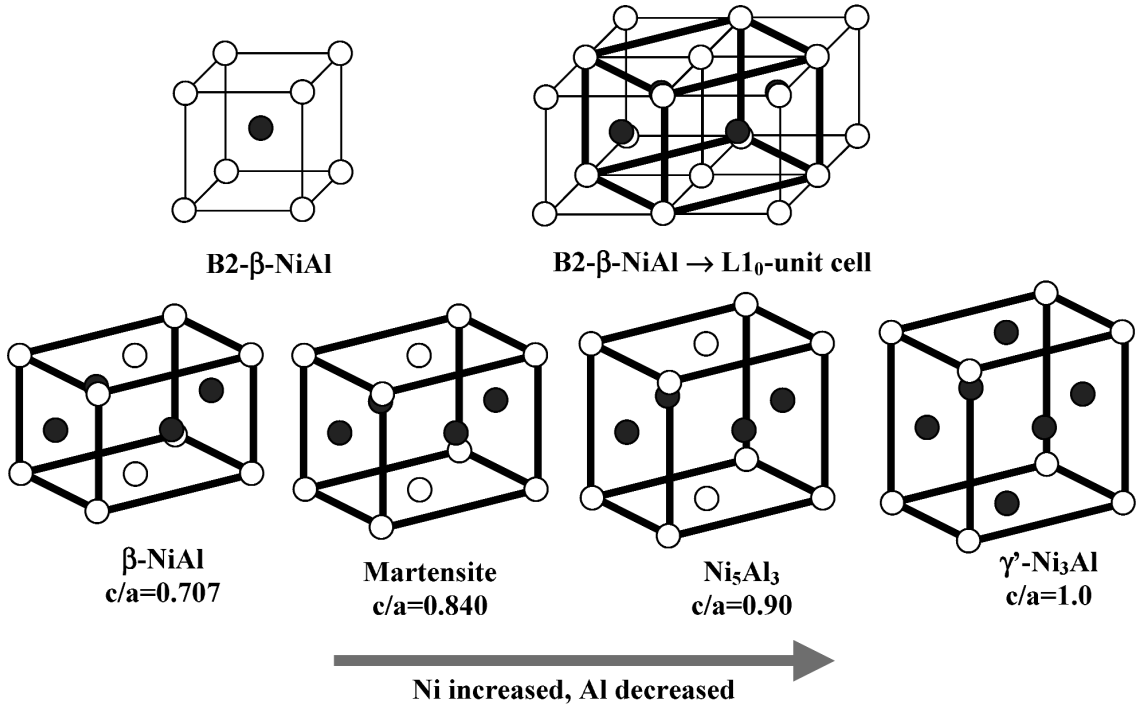

(*c*)

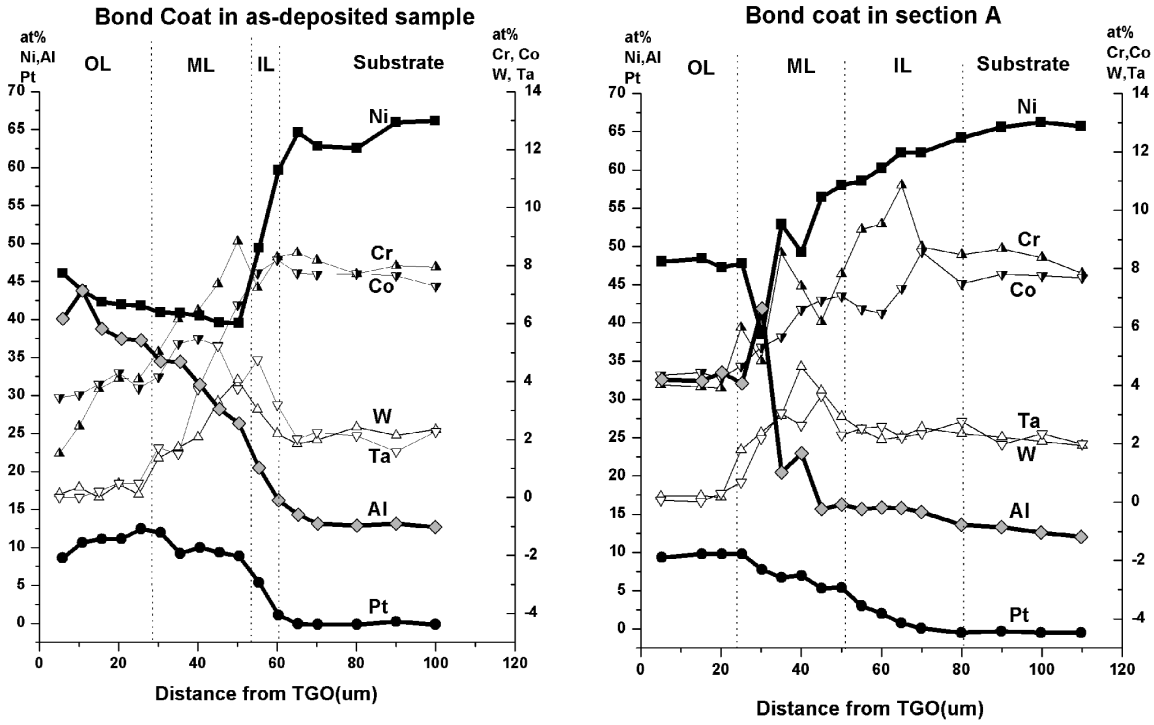

(*d*)

Fig. 8—(Continued). (*a*) Schematic drawing showing interdiffusion in the bond coat during service; diffraction patterns from β-NiAl in the outer layer from various sections are shown in (*b*), while (*c*) shows schematic drawings of the transition from β-NiAl (B2 structure) to γ'-Ni_3Al (Ll_2 structure). Of course, the martensite and Ni_5Al_3 will have some Ni atoms randomly occupying Al sites, and not the 1:1 stoichiometry shown here. (*d*) Composition profiles through the bond coat for the as-deposited material and for Section A.

in the upper left; we can also represent this structure by reference to the L1o structure (upper-right and lower-left sketches). In this latter representation, there is a smooth variation of the *c*/*a* ratio from 0.707 $\left(\sqrt{2}/2\right)$ for NiAl to 1.0 for Ni_3Al. As the Ni concentration increases, transformation to a martensitic structure with $c/a = 0.840$ occurs at a critical Ni concentration, thought to be 50 to 60 at. pct, and then to another ordered phase, Ni_5Al_3, with $c/a = 0.90$.

Table III. Summary of EDS Analysis of Used Blade (Concentrations in Atomic Percent)

	Matrix
Inner layer	γ'—$Ni_{66}Al_{13}Ta_7Co_7Cr_3Pt_3$
Middle layer	β—$Ni_{50}Al_{28}Pt_{12}Co_5Cr_4$
Outer layer	β—$Ni_{45}Al_{26}Pt_{14}Co_5Cr_5Ta_5$
	Precipitates
Inner layer	σ—$Cr_{44}Ni_{17}Co_{16}W_9Re_8Mo_6$
	σ'—$Cr_{42}Ni_{16}Co_{14}W_{10}Re_{10}Mo_6$
	$M_{23}C_6$—$Cr_{74}Ni_6W_5Re_4Ta_4Co_3Mo_2$
Middle layer	μ—$Cr_{20}Ni_{18}Co_{15}W_{13}Ta_{13}Re_{10}Mo_7Pt_3$

Figure 8(d) shows composition profiles from the outer layer to the γ/γ' substrate for the as-deposited sample and for section A. We made sure that the thinnest parts of the TEM foils were used for these analyses. (All the concentrations given derive from quantification of EDS spectra with a thin-film ZAF correction; the absolute accuracy is ~10 pct.) Table I shows the composition of selected phases in the as-received samples and in sections F and A. A more succinct description of the average composition of the three layers and the several precipitates is shown in Table III. In the as-deposited sample, the highest Al concentrations were found in the outer layer, and the concentration decreased from ~40 at. pct in the outer layer to ~15 at. pct in the substrate. In contrast, the Ni concentration increased from ~43 at. pct in the outer layer to ~65 at. pct in the substrate. It is worth emphasizing that the Ni and Al concentrations changed abruptly within the thin inner layer of the as-deposited sample.

The highest Pt concentration was also found in the outer layer, reaching a mean value of ~12 at. pct. The Pt concentration decreased with increasing distance from the TGO, such that finally no Pt exists in the substrate. Similarly, an abrupt decrease in the Pt concentration also occurred within the inner layer. Recognizing the detection limit of the EDS system, just-detectable amounts of Cr and Co (1 to 2 at. pct) were found in the outer layer. The W and Ta concentrations were nearly zero in the outer layer, consistent with the absence of any fine α W particles (Figure 2(a)).

As shown in Figure 8(d), the concentration of these elements changed significantly in various layers of section A. In the outer layer, the mean Al concentrations decreased to ~33 at. pct; the Ni concentrations increased to ~48 at. pct; and the Pt concentrations decreased slightly. The width of the inner layer increased during service, as shown in Table II.

IV. DISCUSSION

In addition to the temperature dependence of interdiffusion between the bond coat and substrate during service, the microstructures in the bond coat are also related to the initial coating microstructures, which depend on the "aluminization" variables utilized in the coating process, primarily time and temperature.[34] The as-deposited bond coat has two main features: (1) the β phase in the outer and middle layers (with the B2 structure) is Al deficient (Table I) and displays a tweed morphology; and (2) the gradient of the Ni concentration is much steeper than that of Al and Pt in the inner layer. Furthermore, the location of the alumina grit particles is consistent with the coating being produced by a low-activity, Ni-outward diffusion process.

The general interdiffusion process in each section of the service blade can be summarized as follows. The Ni-to-Al ratio in both the middle and outer layers increased as Ni diffused outward from the substrate and inner layer. This Ni depletion results in the extension of the γ' inner layer into the substrate. The Ni-rich γ phase in the substrate near the inner layer transformed to γ' due to such interdiffusion. This transformation was accompanied by simultaneous formation of the more Cr-, Co-, and W-rich σ, σ', and $M_{23}C_6$ phases in the newly formed γ' phase. This is possible because the γ' phase dissolves less Cr, Co, and W than the γ phase.[19] Second, this interdiffusion causes the $\beta \rightarrow \gamma'$ phase transition in the middle layer and decreases the volume fraction of the W- and Ta-rich μ particles in the middle layer, because the γ' matrix usually dissolves more W and Ta in the middle layer than does the β matrix.[19]

The β phase is usually considered to be a very good Al_2O_3 former, whereas the γ and γ' phases are poorer oxide formers, which impairs the overall coating performance.[6] The Ni-to-Al ratio in the outer layer increases with interdiffusion, eventually reaching such levels that the β matrix transforms to γ'. In our used blade, no γ' phase was formed, and most of the β phase remained stable in the outer layer of each section. The initial tweed microstructure of the β phase remained for most of the cooler sections. The β stability can possibly be attributed to the absence of any W-rich particles in the initial outer layer. (It was reported that W-rich particles accelerate nucleation of the γ' phase and destabilize the β phase.[35]) The major change we observed is the broken symmetry in the β phase, implying structural modulation of this phase due to small compositional variations. In the hottest section, the martensite that formed can be considered an intermediate structure between the β and γ' phases; the formation of martensite upon cooling results from the large Al depletion during the rapid interdiffusion in the hotter sections. This result is consistent with data in a series of recent articles.[20–23,36] The martensitic transformation affects the mechanical behavior by producing a linear transformation strain,[20,21,36] and it appears to enhance the intermediate-temperature strength of the bond coat.[23]

V. CONCLUSIONS

We have performed a comprehensive microstructural study on an actual turbine blade produced by GE Aircraft Engines and taken out of service after a modest (but unknown) fraction of life. Our SEM/TEM study provides comprehensive information on the microstructures of a widely used bond coat system and its evolution during high-temperature service. As such, it provides an important baseline for improved airfoils in gas turbine systems and a benchmark for assumptions regarding phase evolution in the bond coat.

Specifically, the as-formed bond coat consists of three layers: an inner layer adjacent the Ni-based superalloy, which is a mixture of γ and γ' phases but contains numerous μ and σ precipitates; a middle layer of a β-(Ni,Pt) aluminide containing μ precipitates; and an outer layer of single-phase β-(Ni,Pt) aluminide. An α-Al_2O_3 TGO abuts the outer layer, on which resides the ZrO_2-based thermal barrier coating. During service, spatially varying microstructural changes occur, depending on the spatially varying thermal history of each portion of the turbine blade. Due to interdiffusion, the inner layer extends into the γ/γ' substrate, and some $M_{23}C_6$ carbides

form. The β matrix in the inner layer transforms to a β/γ' mixture, and the various precipitate phases undergo coarsening. The outer layer remains single-phase β, but diffusionally induced composition changes cause the hottest sections to undergo a martensitic transformation on cooling. In the blade we studied, the thickest TGO was ~1.4 μm.

ACKNOWLEDGMENTS

We acknowledge Dr. Joe Rigney, GE Aircraft Engines, for the provision of the used air foil, and Dr. Carlos Levi, UCSB, for his careful reading of a draft of this article. This work was supported by ONR, Dr. Steve Fishman, program manager.

APPENDIX—LATTICE SYMMETRY OF σ'

The lattice symmetry of the σ' phase was determined as follows. A precipitate in an orientation close to a low-index zone axis was assumed to be parallel to c^*. This precipitate was then tilted around c^* to a number of nearby zone axes, and additional diffraction patterns were recorded, as shown in Figure A1. Analysis of these diffraction patterns led to the reciprocal lattice shown in Figure A2, from which it is clear that the structure is orthorhombic, with the lattice parameters $a \sim 1.02$ nm and $b \sim 0.83$ nm. Further tilting experi-

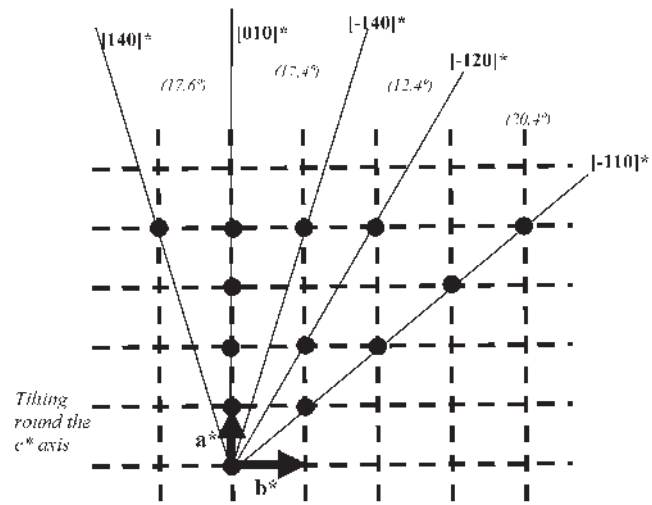

Fig. A2—Construction of the reciprocal lattice based on analysis of the diffraction patterns in Fig. A1.

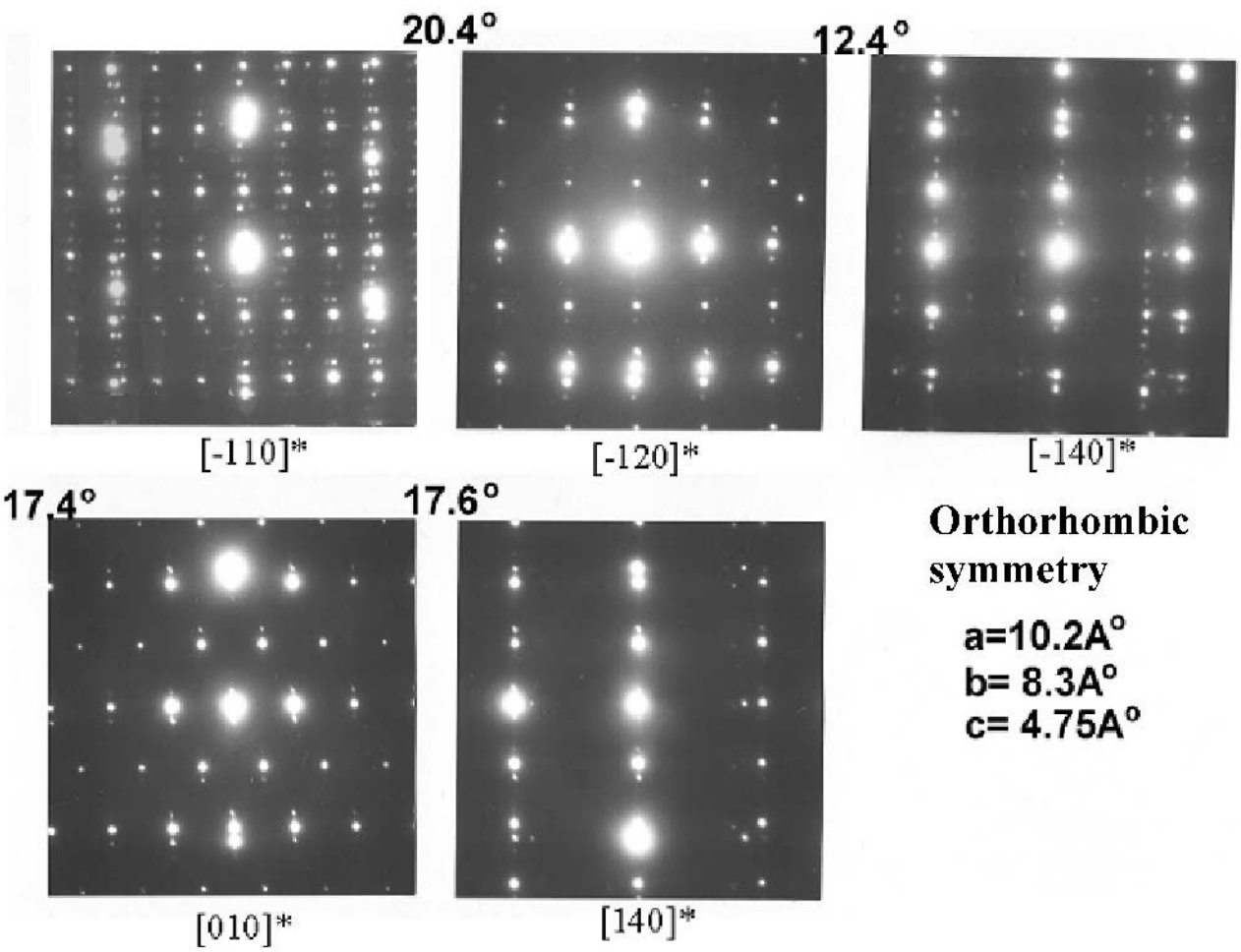

Fig. A1—A series of diffraction patterns from a σ' precipate with orthorhombic symmetry.

ments then allowed the c-axis length to be determined: $c \sim 0.475$ nm.

REFERENCES

1. M. Gobel, A. Rahmel, and M. Schutze: *Oxid. Met*., 1994, vol. 41(3-4), pp. 271-300.
2. J.H. Sun, H.C. Jang, and E. Chang: *Surf. Coating Technol*., 1994, vol. 64, pp. 195-203.
3. W.T. Wu, A. Rahmel, and M. Schrorr: *Oxid. Metall*., 1984, vol. 22, pp. 59-81.
4. J.G. Fountain, F.A. Golightly, F.H. Scott, and G.C. Wood: *Oxid. Metall*., 1976, vol. 10, pp. 341-50.
5. H.M. Tawancy, N.M. Abbas, and T.N. Rhys-Jones: *Surf. Coating Technol*., 1991, vol. 49, pp. 1-7.
6. Y. Niu, W. Wu, D. Boone, J. Smith, J. Zhang, and C. Chen: *J. Phys*., 1993, vol. 3, pp. 511-20.
7. E. Felten: *Oxid. Met*., 1976, vol. 10, pp. 23-41.
8. E. Felten and F. Pettit: *Oxid. Met*., 1976, vol. 10, p. 189.
9. P. Tomaszewicz and G.R. Wallwork: in *Reviews of High Temperature Materials*, J. Newkirk, ed., Freund Publishing House, London, 1982, p. 49.
10. W.F. Gale and J.E. King: *Surf. Coating Technol*., 1992, vols. 54–55, pp. 8-12.
11. J. Angenete and K. Stiller: *Mater. Sci. Eng*., 2001, vol. A316, pp. 182-94.
12. J. Angenete: Licentiate Thesis, Chalmers University of Technology and Goeteborg University, Göteborg, Sweden, 1999.
13. J.H. Chen and J.A. Little: *Surf. Coating Technol*., 1997, vol. 92, pp. 69-77.
14. E. Basuki, A. Crosky, and B. Gleeson: *Mater. Sci. Eng. A*, 1997, vol. 224, pp. 27-32.
15. J.W. Holmes and F.A. McClintock: *Metall. Trans. A*, 1990, vol. 21, pp. 1209-22.
16. P. Moretto and J. Bressers: *J. Mater. Sci*., 1996, vol. 31, pp. 4817-29.
17. H.M. Tawancy, N. Sridhar, N.M. Abbas, and D. Rickerby: *Scripta Mater*., 1995, vol. 33, pp. 1431-38.
18. W.F. Gale and J.E. King: *J. Mater. Sci*., 1993, vol. 28, pp. 4347-54.
19. W.F. Gale and J.E. King: *Metall. Trans. A*, 1992, vol. 23A, pp. 2657-65.
20. M.W. Chen, R.T. Ott, T.C. Hufnagel, P.K. Wright, and K.J. Hemker: *Surf. Coating Technol*., 2003, vols. 163–164, pp. 25-30.
21. M.W. Chen, K.J.T. Livi, P.K. Wright, and K.J. Hemker: *Metall. Mater. Trans. A*, 2003, vol. 34, pp. 2289-99.
22. D. Pan, M.W. Chen, P.K. Wright, and K.J. Hemker: *Acta Mater*., 2003, vol. 51, p. 2205.
23. M.W. Chen, M.L. Glynn, R.T. Ott, T.C. Hufnagel, and K.J. Hemker: *Acta Mater*., 2003, vol. 51, pp. 4279-94.
24. D.P. Garriga-Majo, B.A. Shollock, D.S. McPhail, R.J. Chater, and J.F. Walker: *Int. J. Inorg. Mater*., 1999, vol. 1, pp. 325-36.
25. O. Unal, A.H. Heuer, and T.E. Mitchell: *J. Electron Microsc. Technique*, 1990, vol. 14, pp. 307-14.
26. V.K. Tolpygo and D.R. Clarke: *Acta Mater*., 2000, vol. 48, pp. 3283-93.
27. M.J. Steiger, N.M. Yanar, F.S. Pettit, and G.H. Meier: *Elevated Temperature Coatings: Science and Technology III*, 1999, p. 51.
28. K.S. Murphy, K.L. More, and M.J. Lance: *Surf. Coating Technol*., 2001, vols. 146–147, pp. 152-61.
29. U. Schulz, M. Menzebach, C. Leyens, and Y.Q. Yang: *Surf. Coating Technol*., 2001, vols. 146–147, pp. 117-23.
30. C.G. Levi, E. Sommer, S.G. Terry, A. Catanoiu, and M. Rühle: *J. Am. Ceram. Soc*., 2003, vol. 86 (4), pp. 676-85.
31. O. Unal, T.E. Mitchell, and A.H. Heuer: *J. Am. Ceram. Soc*., 1994, vol. 77 (4), pp. 984-92.
32. U. Schulz and M. Schücker: *Mater. Sci. Eng*., 2000, vol. A276, pp. 1-8.
33. J.C. Schaeffer: *Proc. NASA TBC Workshop*, May 19–21, 1997, NASA, Cleveland, OH, 1997, p. 99.
34. S. Shankar: Ph.D. Thesis, State University of New York, 1977.
35. J. Angenete and K. Stiller: *Mater. Sci. Eng*., 2001, vol. A316, pp. 182-94.
36. Y. Zhang, J.A. Haynes, B.A. Pint, I.G. Wright, and W.Y. Lee: *Surf. Coating Technol*., 2003, vols. 163–164, pp. 19-24.